# Supplementary Information

# Improving signal-to-background ratio by orders of magnitude in high-speed volumetric imaging in vivo by robust Fourier light field microscopy

JIAZHEN ZHAI[1,†], RUHENG SHI[1,†], AND LINGJIE KONG[1,2, *]

*[1]Department of Precision Instrument, State Key Laboratory of Precision Measurement Technology and Instruments, Tsinghua University, Beijing 100084, China*

[2]*IDG/McGovern Institute for brain research, Tsinghua University, Beijing 100084, China*

*\*konglj@tsinghua.edu.cn*

[†]*Contributed equally to this work as first authors.*

# Supplementary Figures

## 1. System design

**Fig. S1.** Schematic of structured illumination modulation.

**Fig. S2.** Raw images of larval zebrafish captured under RFLFM.

**Fig. S3.** Procedure of data processing in RFLFM and FLFM.

## 2. Experimental results

**Fig. S4.** High-contrast volumetric imaging of vascular structure in zebrafish *in vivo*.

**Fig. S5.** Neuronal network activities in Fig. 2c.

**Fig. S6.** Statistic of SBR improvement of neurons in larval zebrafish *in vivo*.

**Fig**. **S7.** Contrast improvement of neuron detection in Fig.2.

**Fig. S8.** Visualization 1 annotation. Neuron activity in brains of larval zebrafish *in vivo*.

**Fig. S9.** Visualization 2 annotation. Heart-beating imaging of larval zebrafish (RFLFM mode) *in vivo*.

**Fig. S10.** SBR improvement in vascular dilation imaging.

**Fig. S11.** Visualization 3 annotation. Vascular dilations in mouse brains *in vivo*.

**Fig. S12.** Neuronal network activities in Fig. 5d.

**Fig. S13.** Visualization 4 annotation. Neuronal network activity in mouse brains *in vivo*.

**Fig. S14.** Clustering of neurons in mouse cortex *in vivo* based on their fluorescence dynamics.

**Fig. S15.** Statistic of SBR improvement of neurons in mouse cortex *in vivo*.

**Fig. S16.** RFLFM eliminates the background-fluctuation induced artifacts.

## 3. System calibration

**Fig. S17.** Raw point-spread-function (PSF) stack projection.

**Fig. S18.** Enlarged view of PSF and estimation of resolution.

**Fig. S19.** Experimental calibration of the system resolution.

**Fig. S20.** The *x-y*, *y-z*, *x-z* views and the FWHM of the two fluorescent beads in Fig.S19.

**Fig. S21.** Statistical optical resolution of the system.

**Fig. S22.** Rays tracing based simulation of the aberrations.

**Fig. S23.** Simulation of resolutions in samples of different densities.

**Fig. S24.** Comparison between raw PSF and PSF after HiLo. $C_s(\vec{\rho})$=0.2, $\eta$=1.5.

# Supplementary Notes

**Supplementary Note 1:** Design of RFLFM.

1. Design of FLFM.

2. Design of HiLo.
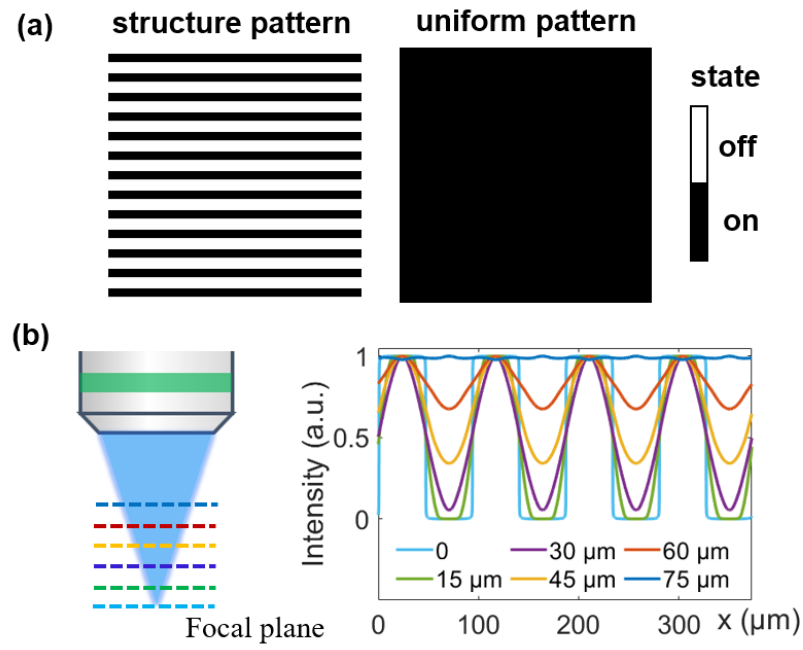
# Supplementary Reference

Fig. S1. Schematic of structured illumination modulation. (a). The grid structured pattern and uniform pattern displayed on the DMD, switched in turns. (b). The illumination patterns are projected on the native object plane (NOP). For the structured illumination, the pattern contrast decreases as the defocus distance increases. We show the normalized intensity profile at varies depths for the structured pattern in Fig. S1b, based on numerical simulations[1].
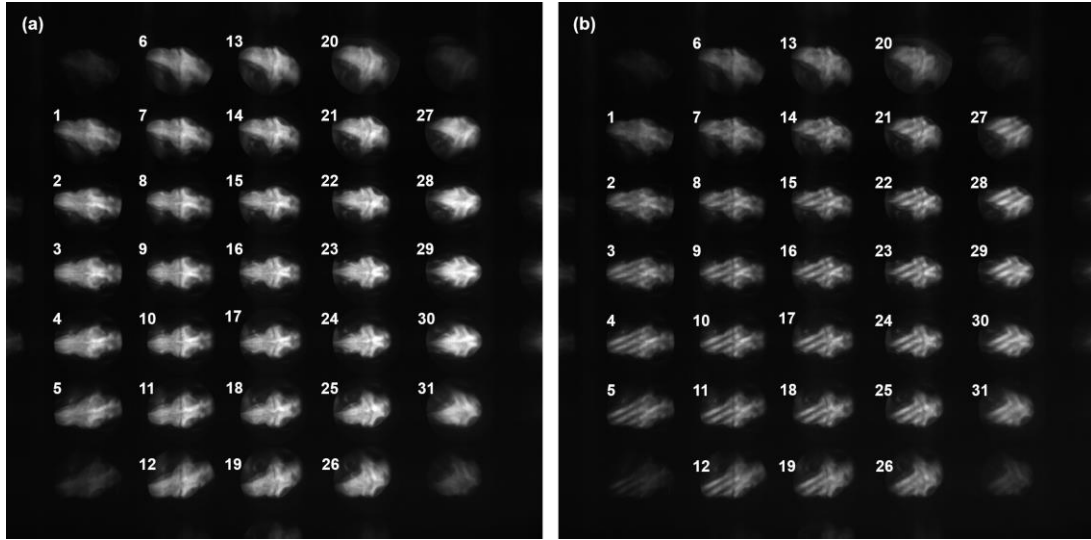
Fig. S2. Raw images of larval zebrafish captured under RFLFM. (a). Raw image captured under uniform illumination. (b). Raw image captured under grid structured illumination. The numbers label on both Fig. S2a and Fig. S2b note the sub-images of different views, which are corresponding to the different lens of microlens array (MLA). The total pixel numbers are 5120×5120, we divide 666×666 pixels for each sub-image.
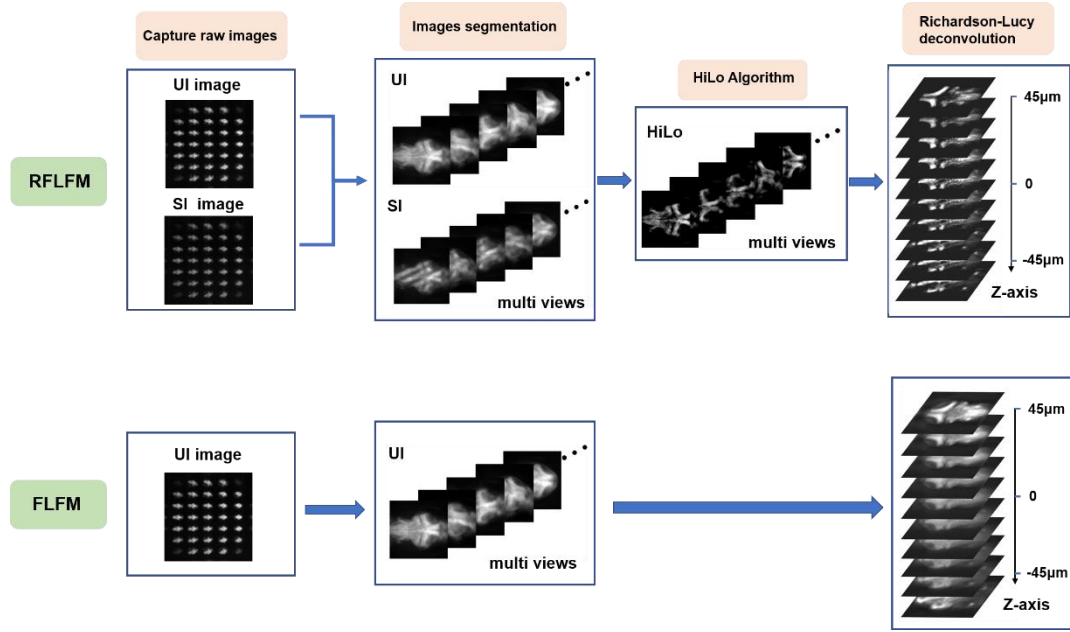
Fig.S3. Procedure of data processing in RFLFM and FLFM. UI: uniform illumination, SI: structured illumination. After acquiring raw images under structure illumination and uniform illumination sequentially, we firstly divide the whole images to sub-images in multi-views (31 views). In RFLFM, we use the HiLo algorithm [2] to achieve optical-sectioning sub-images for all views, thus, we get the high contrast images. Finally, we employ the Richardson-Lucy deconvolution [3, 4] method to reconstruct the volumetric images. In FLFM, we directly use the multi-views UI images to reconstruction the volumetric images.
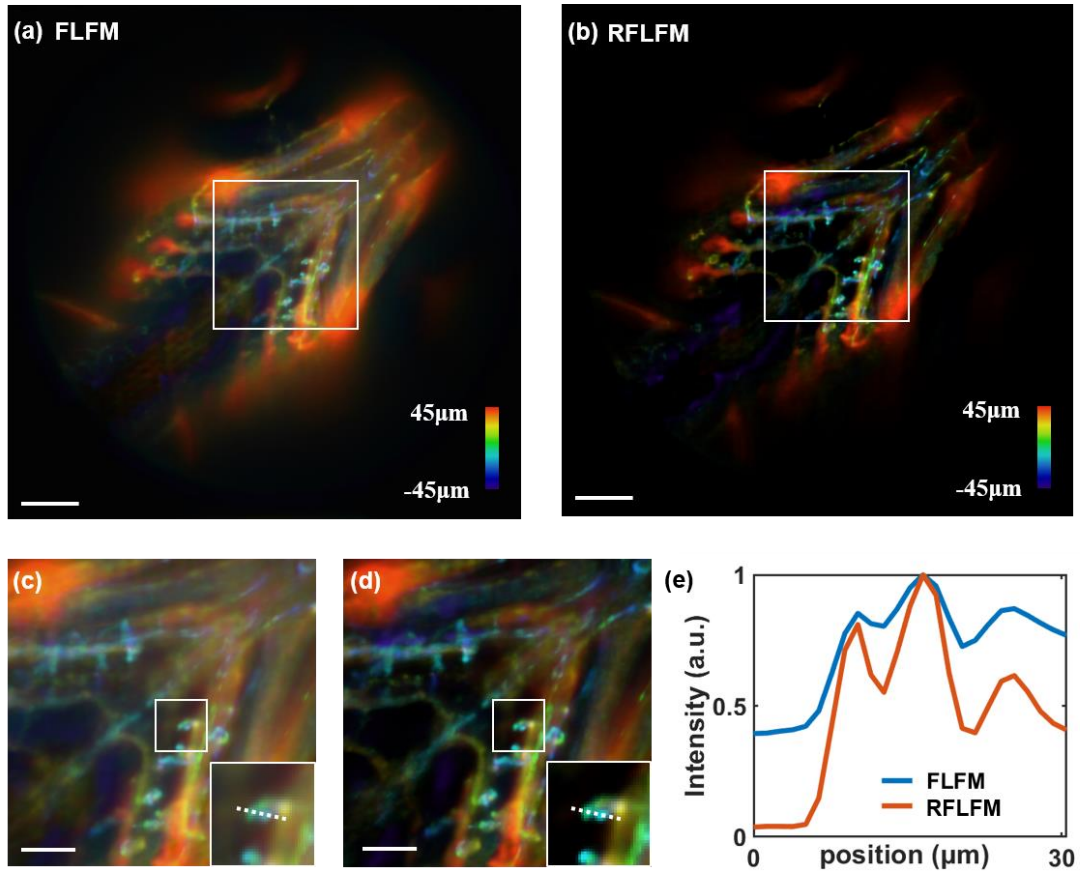
Fig.S4. High-contrast volumetric imaging of vascular structure in zebrafish *in vivo*. (a and b). The imaging depth is centered at about tens of microns below the body surface of zebrafish. Volumetric images of zebrafish vascular structure achieved by FLFM and RFLFM, respectively. Color coded depth. Scale bar: 100 μm. (c and d). Enlarged image in white boxes in Fig. S4(a and b), respectively. Color coded depth. Scale bar: 50 μm. (e). Profiles along the white dotted lines in Fig. S4(c and d). Blue: for FLFM, Orange: for RFLFM. The results suggest RFLFM provide higher contrast for structural imaging compared to that in FLFM, with the contrast and signal-to-background ratio (SBR) improve as much as 2.2 and 16.8 times, respectively.
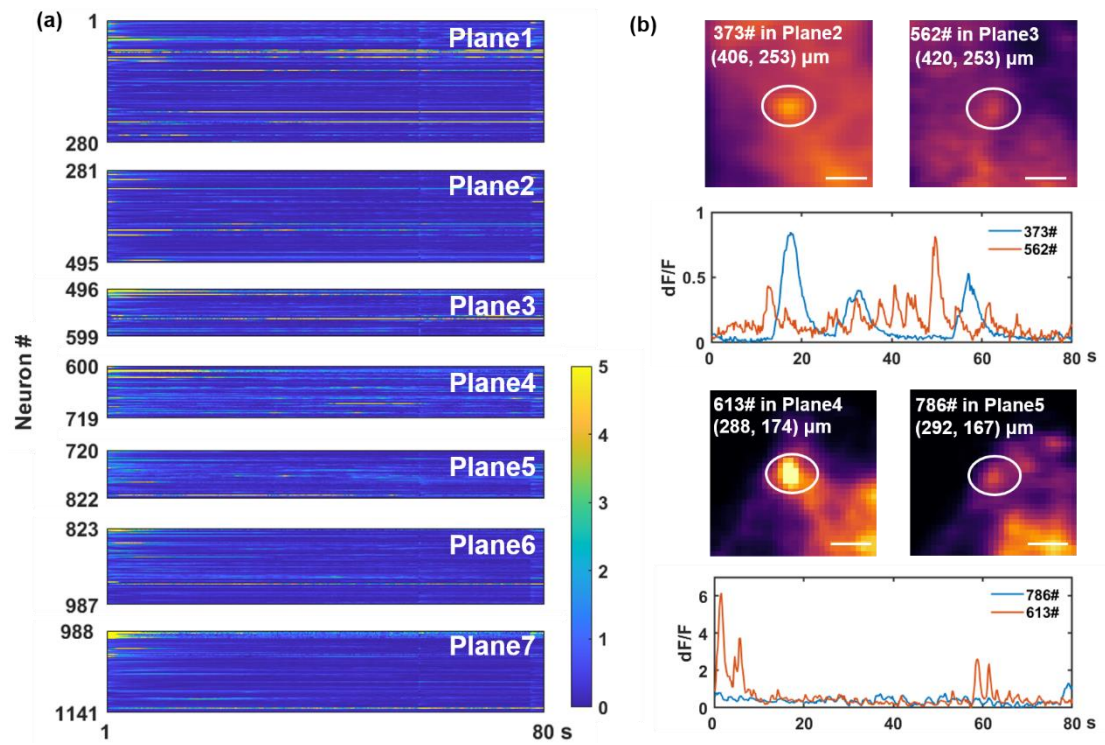
Fig. S5. Neuronal network activities in Fig. 2c. (a). Neuronal network activities of different axial planes in larval zebrafish. The planes 1 to 7 are at z=-45:15:45 μm planes. (b). Comparison of the neuronal activities of adjacent neurons. Scale bar: 10 μm.
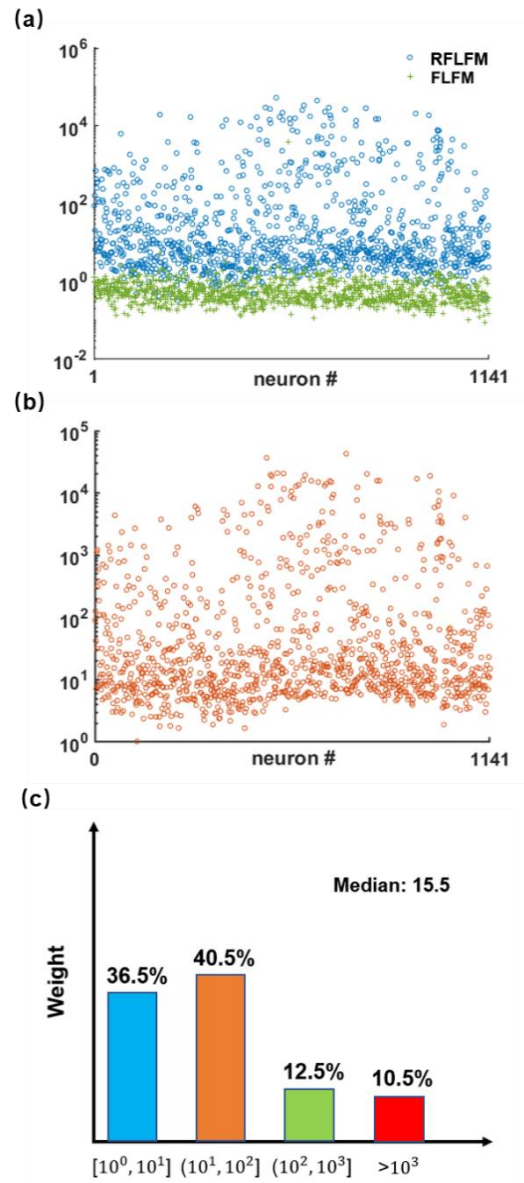
Fig.S6. SBR improvement statistics of neurons in larval zebrafish in vivo. (a). The SBR of each neuron in Fig. 2 in both RFLFM and FLFM modes. (b). SBR improvement of each neurons in Fig.S5a. (c). Statistic results of Fig.S5b.
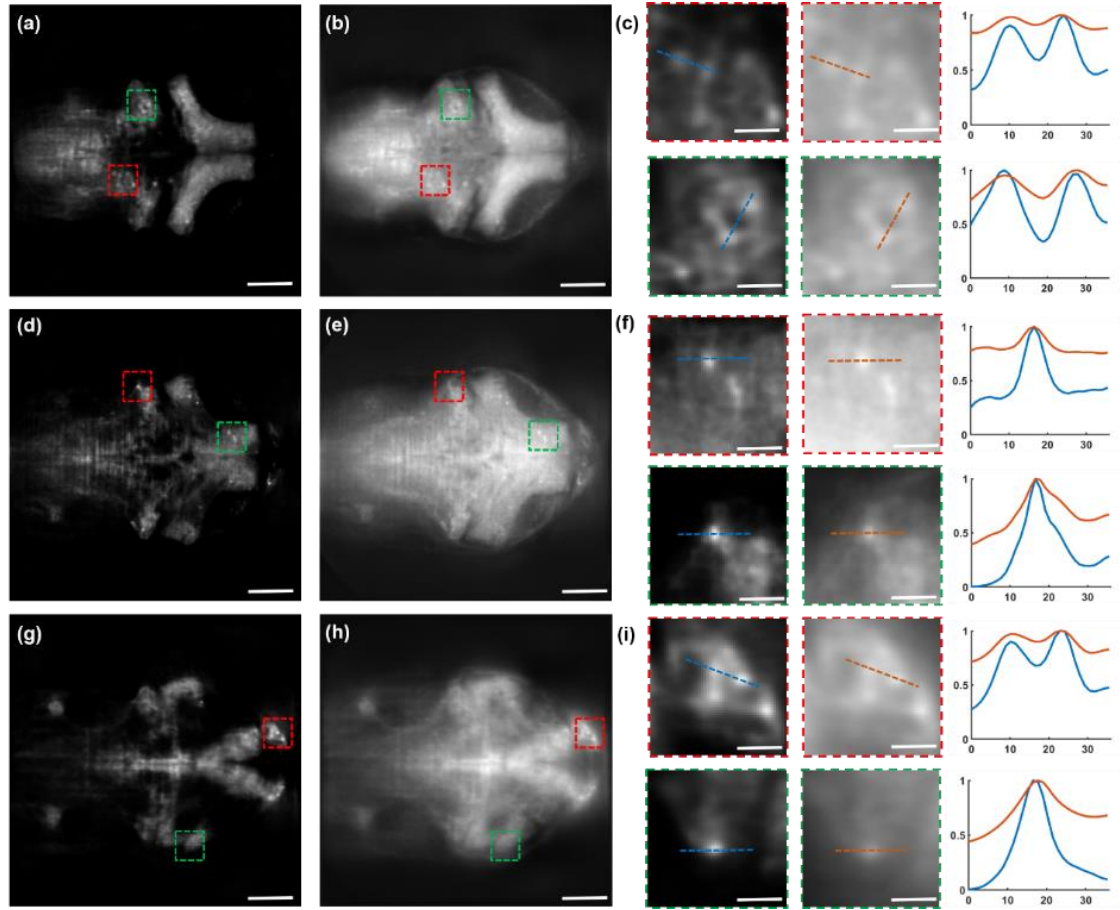
Fig.S7. Contrast improvement of neuron detection in Fig.2. (a, d and g). RFLFM reconstructed images at depths of $z$=30, 0, -30 μm, respectively. Scale bar: 100 μm. (b, e and h). FLFM reconstructed images at depths of $z$=30, 0, -30 μm, respectively. Scale bar: 100 μm. (c, f and i). Enlarged images and profiles for the selected ROIs (labeled with colored boxes) in Figs. S6(a, b, d, e, g and h). Scale bar: 20 μm. The left column is for Figs. S6(a, d and g), and the medium column is for Figs. S6(b, e and h), respectively. The right column shows the profiles across the flashing neurons (dotted lines labeled in the left and medium columns in Figs. S6(c, f and i)), blue lines indicate RFLFM while brown lines indicate FLFM, the vertical axis labels normalized intensity and the horizontal axis labels length with $\mu m$ unit, respectively.
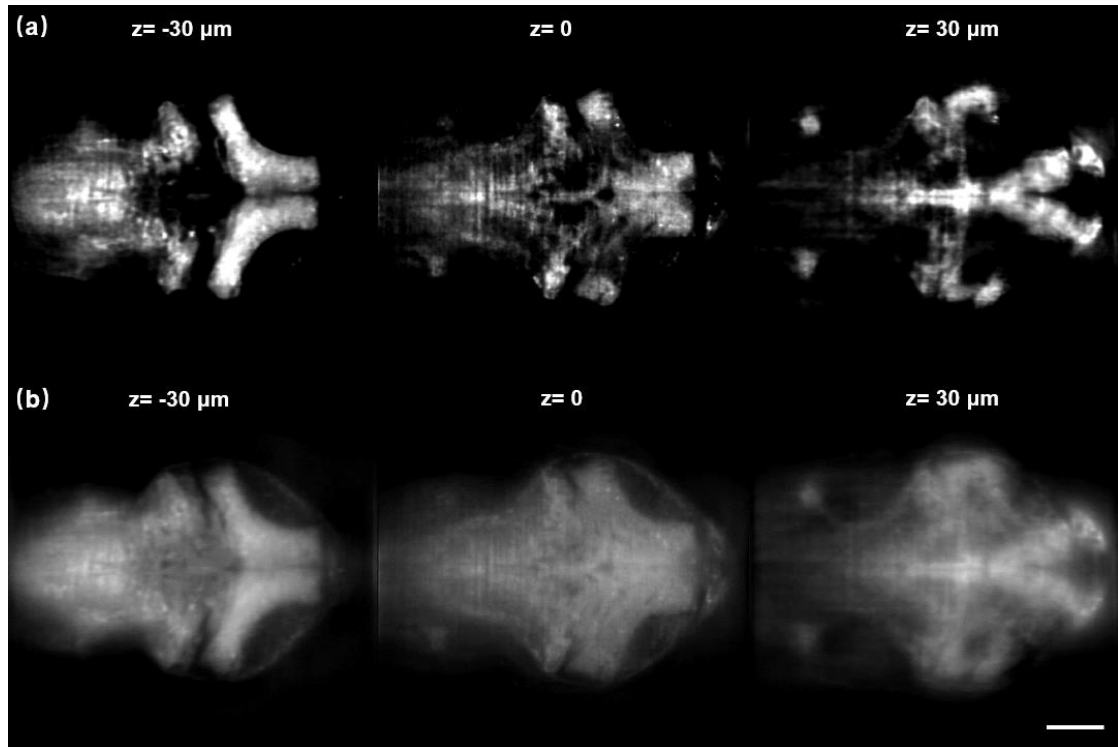
Fig.S8. Visualization 1 annotation. Neuron activity in brains of larval zebrafish in vivo. (a). FLFM reconstructed images, at z= -30, 0, 30 μm from left to right columns, respectively. (b). RFLFM reconstructed images, at z= -30, 0, 30 μm from left to right columns, respectively. The Scale bar: 100 μm. The video is played as 10 times acceleration.
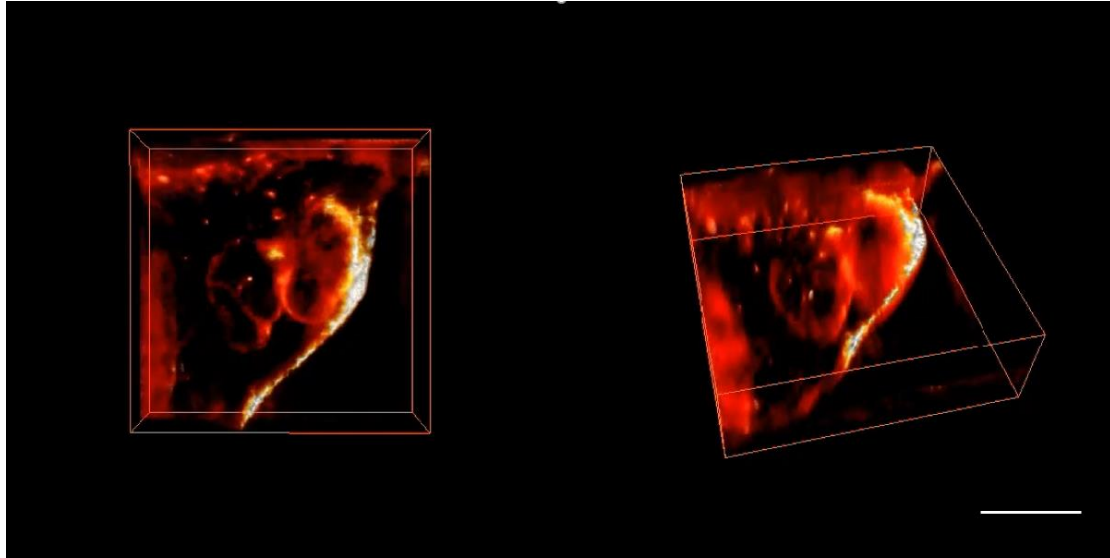
Fig.S9. Visualization 2 annotation. Heart-beating imaging of larval zebrafish (RFLFM mode) in vivo. Scale bar: 100 μm. The video is played with original speed.
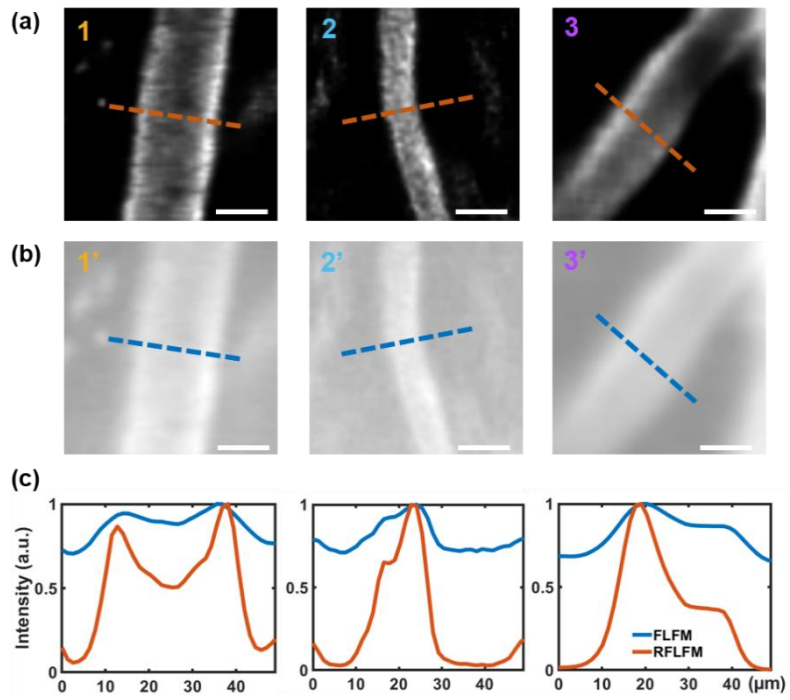
Fig.S10. SBR improvement in vascular dilation imaging. (a). Enlarged images of ROIs 1-3 in Fig.4a, respectively. Scale bar: 20µm. (b). Enlarged images of ROIs 1'-3' in Fig.4b, respectively. Scale bar: 20µm. (c). Profiles of the dotted lines labeled areas in Figs. 4(e and f), where the blue lines indicate RFLFM and brown lines for FLFM.
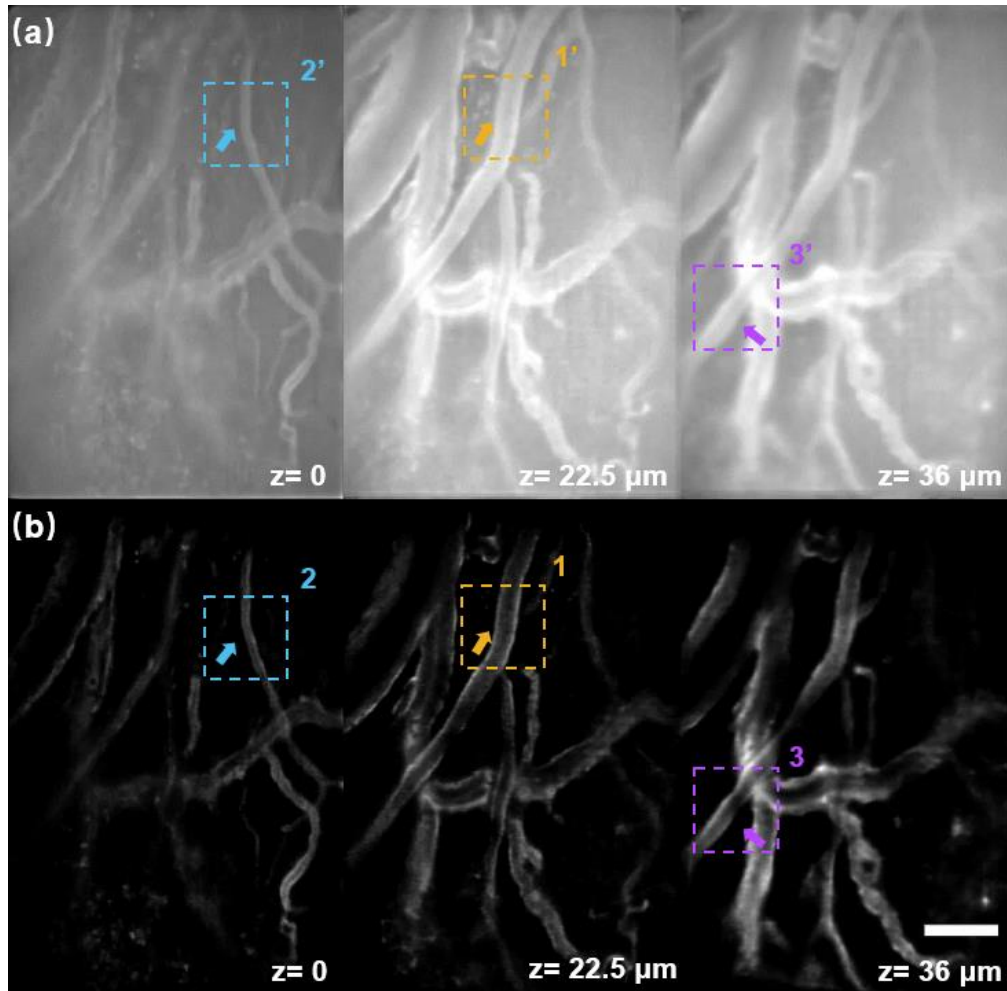
Fig.S11. Visualization 3 annotation. Vascular dilations in mouse brains in vivo. (a). FLFM reconstructed images, we choose ROIs of 670×460 μm2 at z=0, 22.5, 36 μm from left to right columns, respectively. (b). RFLFM reconstructed images, the same ROIs as Fig. S10a, respectively. The Scale bar: 100 μm. The video is played as 5 times acceleration.
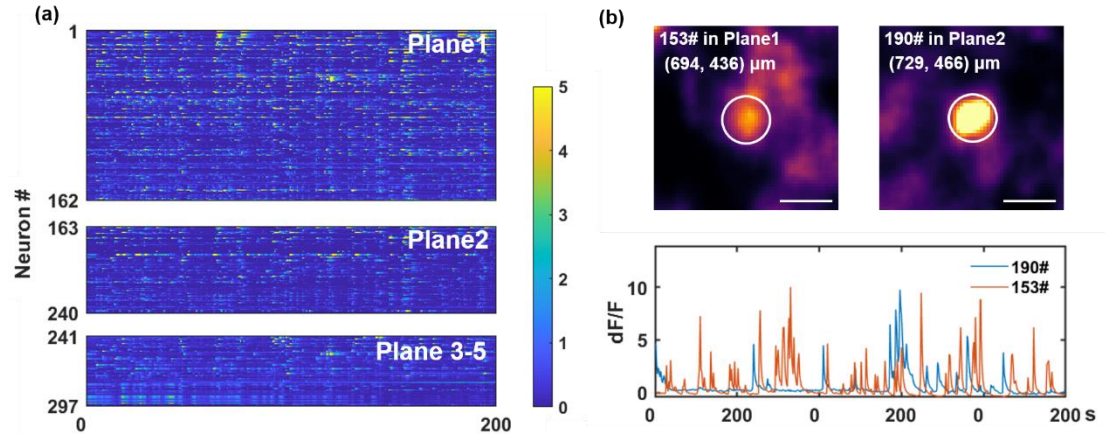
Fig. S12. Neuronal network activities in Fig. 5d. (a). Neuronal network activities of different axial planes in mouse cortex. The planes 1 to 5 are at z=-45:20:35 μm. (b). Comparison of neuronal activities of adjacent neurons. Scale bar: 20 μm.
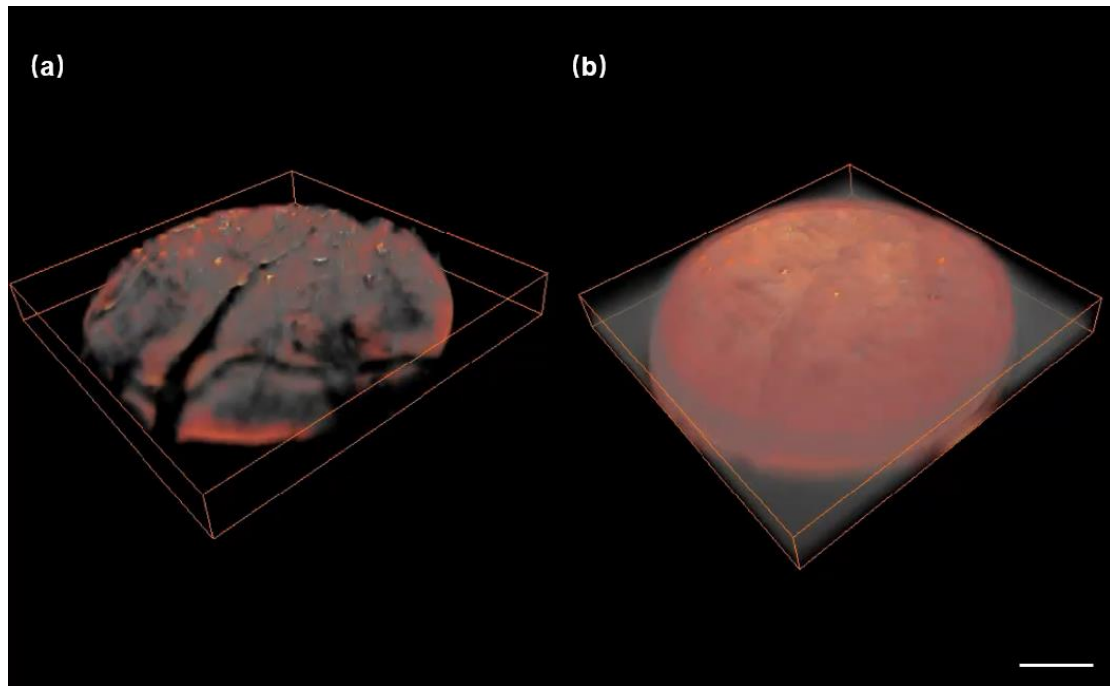
Fig.S13. Visualization 4 annotation. Neuronal network activity in mouse brains in vivo. (a). RFLFM reconstructed images. (b). FLFM reconstructed images. The Scale bar: 200 μm. The MIP images are displayed in gray as a constant and the videos are displayed in color. The video is played as 30 times acceleration.
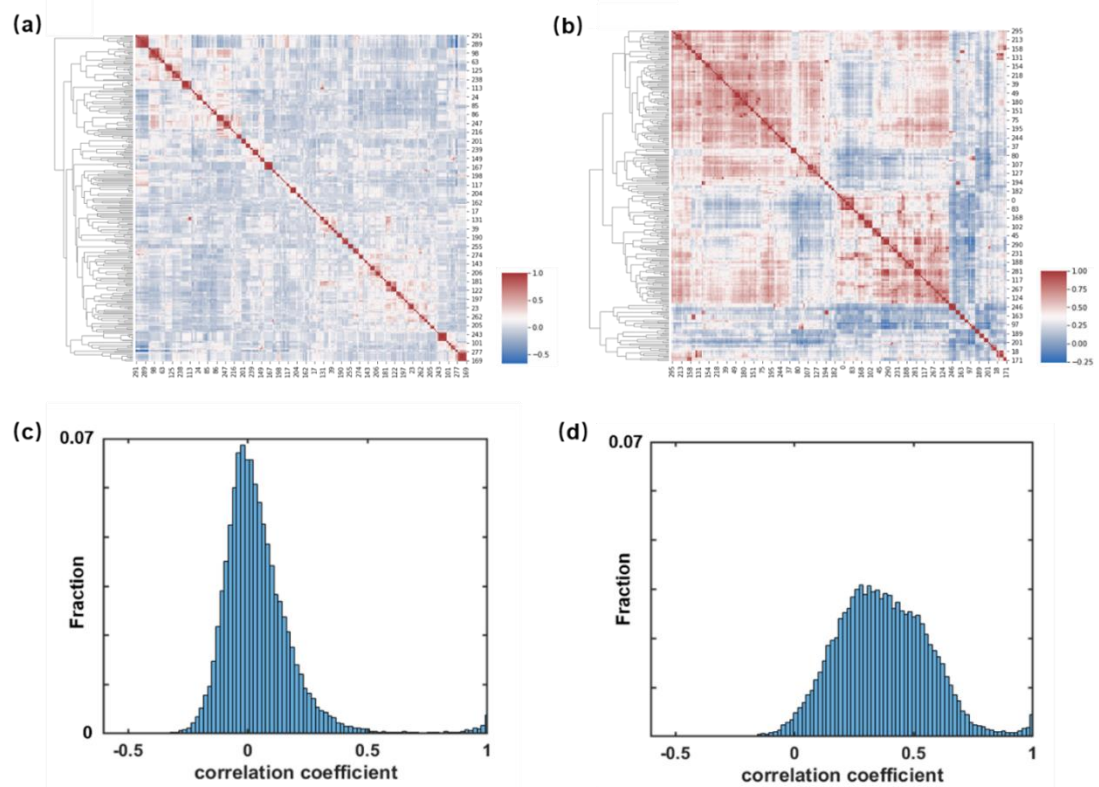
Fig.S14. Clustering of neurons in mouse cortex in vivo based on their fluorescence dynamics. (a). Clustering of neurons in RFLFM mode. (b). Correlation coefficient of neuronal activity dynamics in RFLFM mode. (c). Clustering of neurons in FLFM mode. (d). Correlation coefficient of neuronal activity dynamics in FLFM mode. The results suggest that the natural signals are highly merged by the background-fluctuation induced artifacts in FLFM mode, but show independent signals in RFLFM mode.
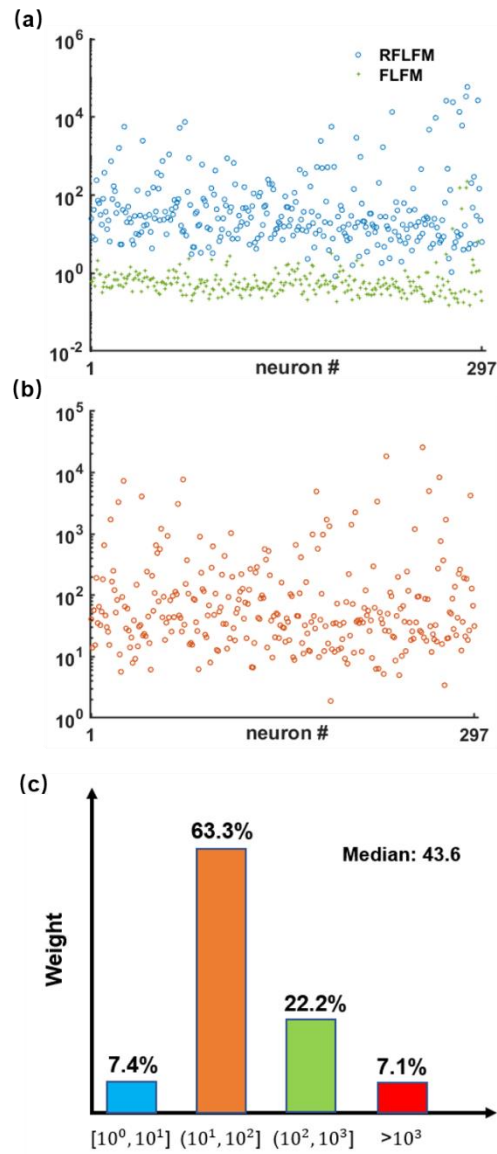
Fig.S15. SBR improvement statistics of neurons in mouse cortex in vivo. (a). The SBR of each neuron in Fig. 5 in both RFLFM and FLFM modes. (b). SBR improvement of each neurons in Fig.S13a. (c). Statistic results of Fig.S13b.
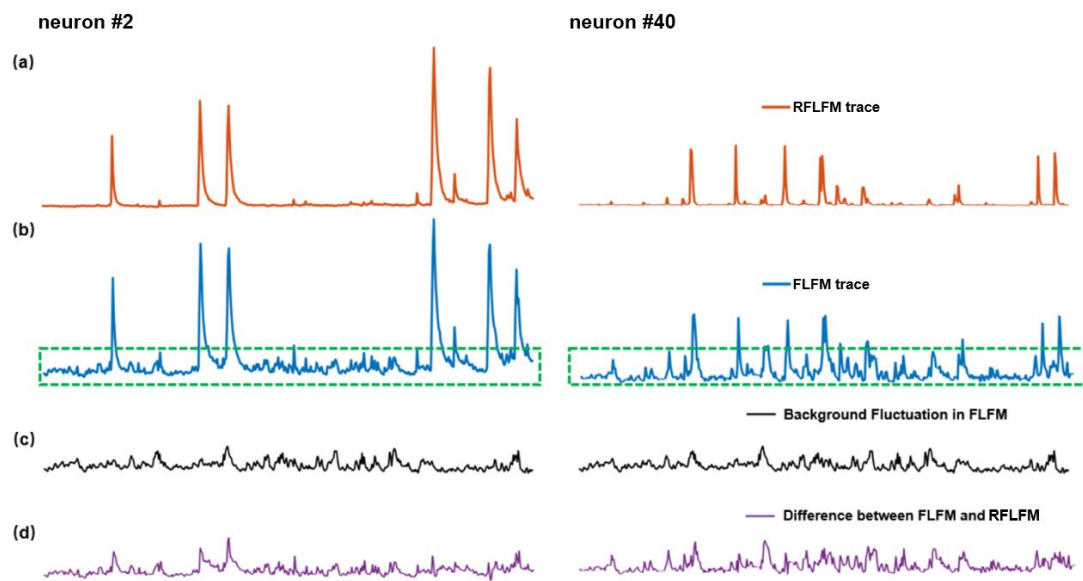
Fig.S16. RFLFM eliminates the background-fluctuation induced artifacts. (a). Temporal traces of neuron #2 and neuron #40 in RFLFM results. (b). Temporal traces of neuron #2 and neuron #40 in FLFM results. (c). Background fluctuation in FLFM (acquired by average the whole FOV pixels for each frame). (d). The difference of temporal traces between FLFM and RFLFM imaging temporal traces of neuron 2 and neuron 40, which are highly correlated to background fluctuation.
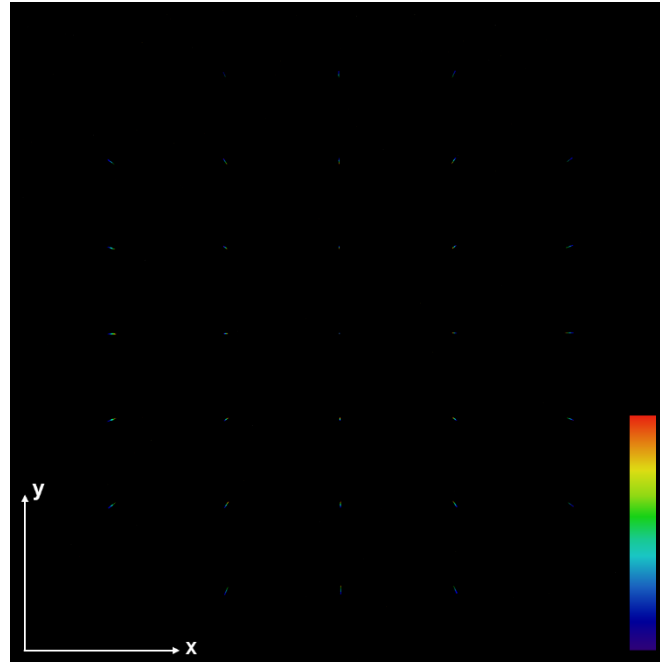
Fig.S17. Raw point-spread-function (PSF) stack projection. We use the Φ=1.1 μm micro-fluorescence beads (Thermo Fisher Scientific) as samples to experimentally calibrate the PSF. We make the sample so sparse that only one bead in our field-of-view (FOV). We image the sample for 60 times with 1.5 μm step. A max intensity projection (MIP) way is employed to show the 3-Dimensional PSF. The PSF projection in x-y plane changes as the defocus depth varies, which exhibits the volumetric information. Color coded depth range from -45μm to 45μm.
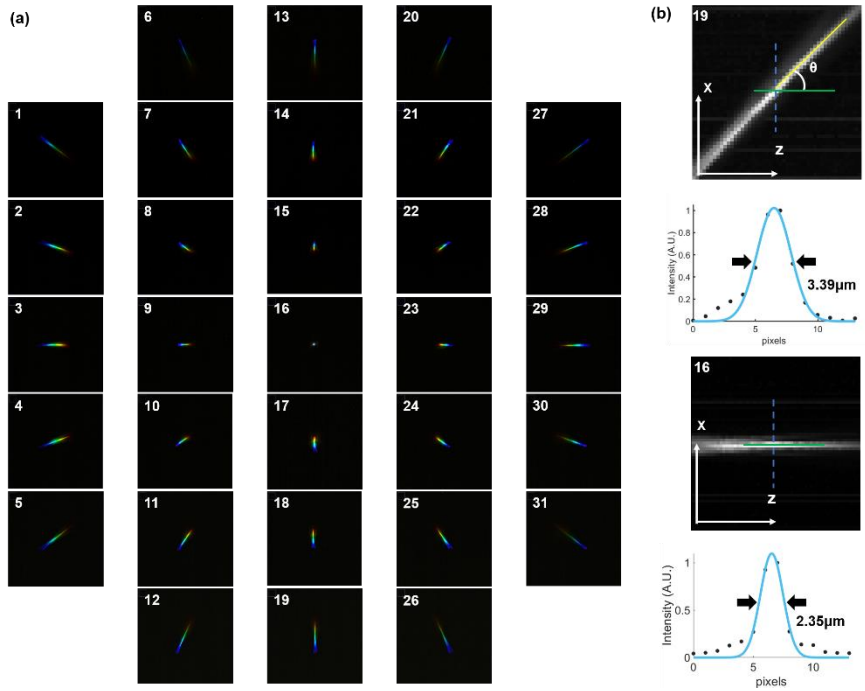
Fig.S18. Enlarged view of PSF and estimation of resolution. (a). 24 times enlarged view of PSF for each view in Fig. S15, the shift of PSF projection in x-y plane is approximately proportion to the distance between the center of corresponding lens and the central axis. (b). The x-z projection of center (number 16) view and an edged (number 19) view, the former could not provide volumetric information due to the invariance of PSF, but the latter provides the axial resolution due to the largest shift in x-y while z moving. The $tg\theta$ is measured to be $0.98 \times \frac{1.5}{1.27}$, and the axial resolution is expected as $R_x \times tg\theta$. However, the image aberration is always more severe in the high frequency domain, which deteriorates the lateral resolution, thus our expected axial resolution is 3.94μm.
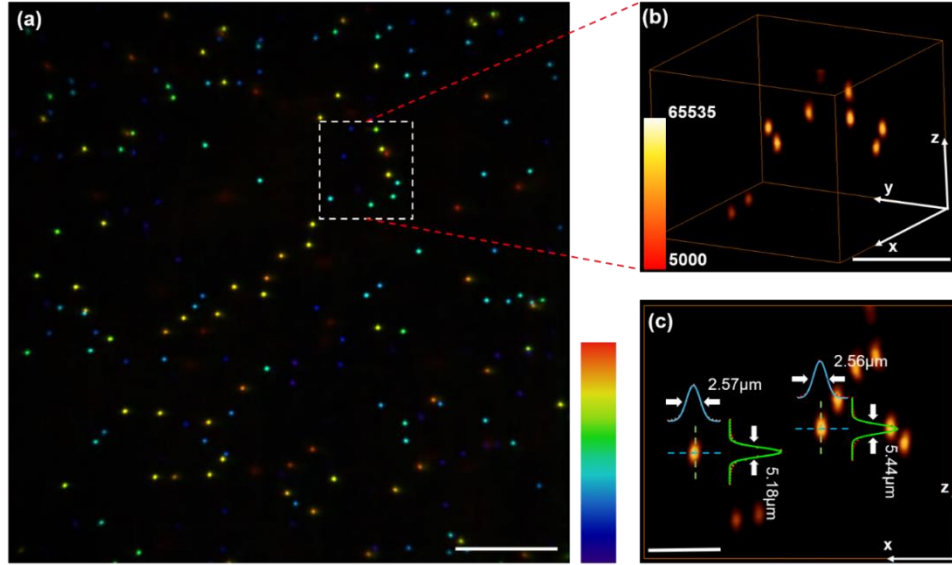
Fig.S19. Experimental calibration of the system resolution. we use Φ=1.1 μm sub-resolution micro-beads (Thermo Fisher Scientific) as samples and Richardson-Lucy deconvolution method for reconstruction. (a). Reconstructed micro-beads, color coded depth from -45μm to 45μm. (b). Enlarged volumetric image of the selected area in Fig. S17a. (c). x-z projection of Fig. S13b. The measured FWHM shows that lateral resolution achieves our expected resolution while axial resolution is slightly worse than the expected resolution due to aberrations.
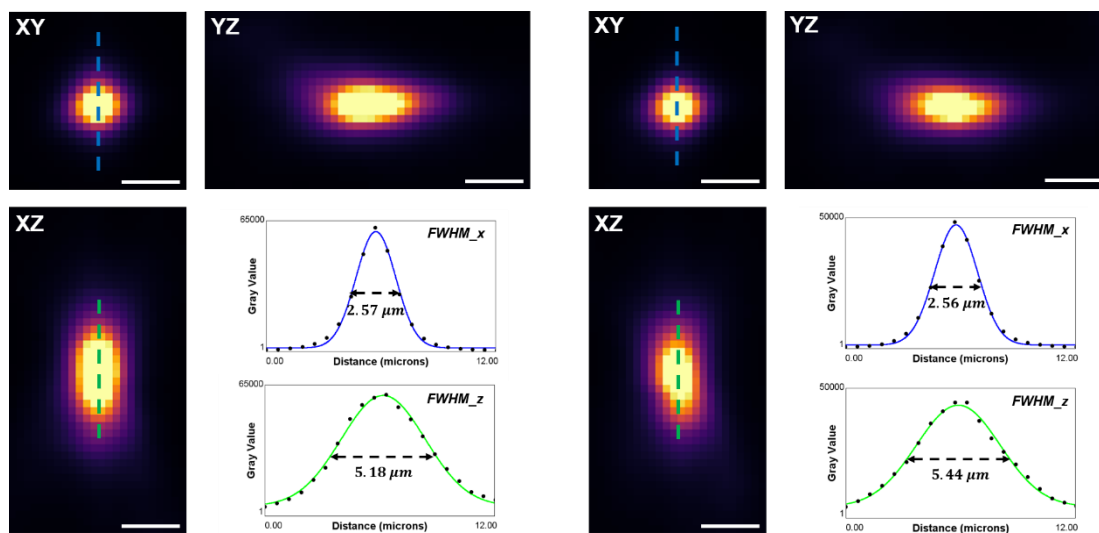
Fig. S20. The *x-y*, *y-z*, *x-z* views and the FWHM of the two fluorescent beads in Fig.S19. Scale bar: 5 μm.
All the images are shown with 2× up-sampling.
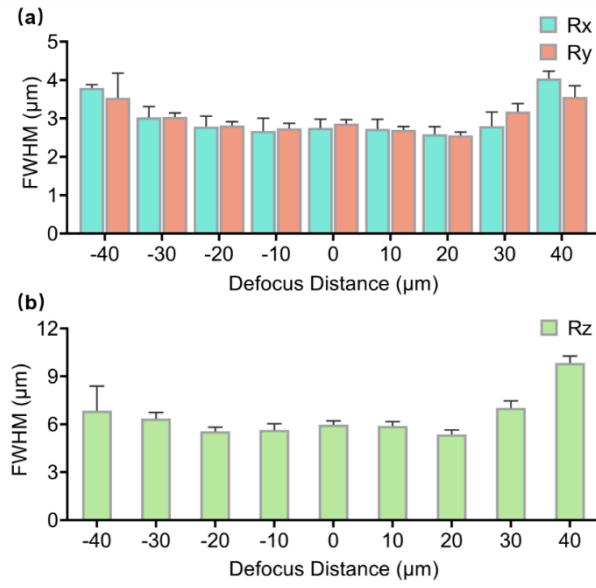
Fig.S21. Statistical optical resolution of the system. We divide the DOF to 9 ranges with 10 μm interval, and perform the statistics of the optical resolution across all FOV. (a). Lateral resolution. (b). Axial resolution. The data are shown with 95% confidence interval.
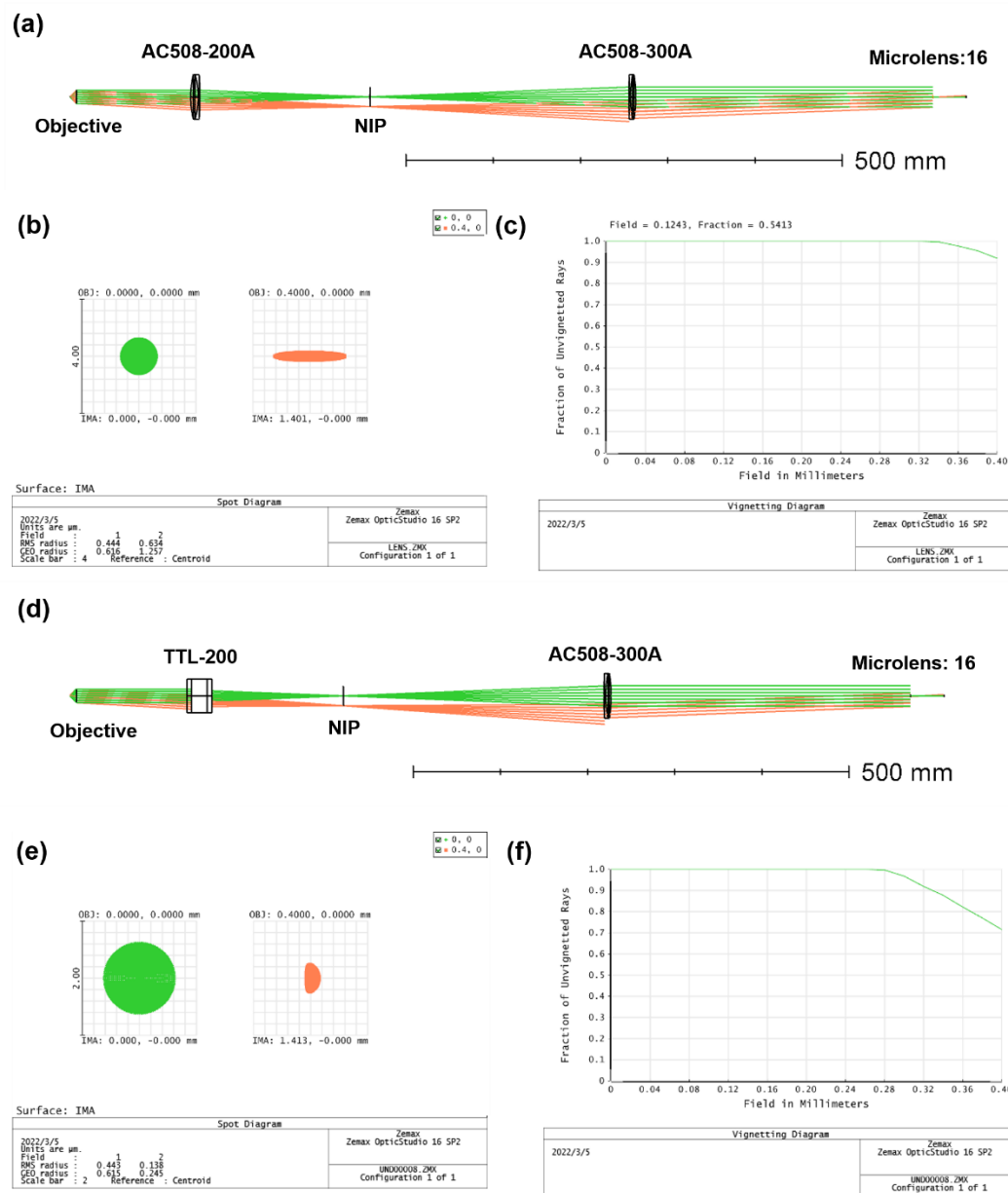
Fig. S22. Rays tracing based simulation of the aberrations. (a). Simulation with the actual optical elements. (b). The focused spots of x=0 and x=400 μm apart from the center of FOV in Fig. S22a. The RMS is 0.444 μm and 0.634 μm in view 16, respectively. (c). The fractions of unvignetted rays in full NA of objective. (d). Simulation with the tube lens replaced the doublet lens. (e). The focused spots of x=0 and x=400 μm apart from the center of FOV in Fig. S22d. The RMS is 0.443 μm and 0.138 μm in view 16, respectively. We note that RMS is smaller on the edge of FOV since the most of rays are cut-off. (f). The fractions of unvignetted rays in full NA of objective, which is much more serious than Fig. S22c.
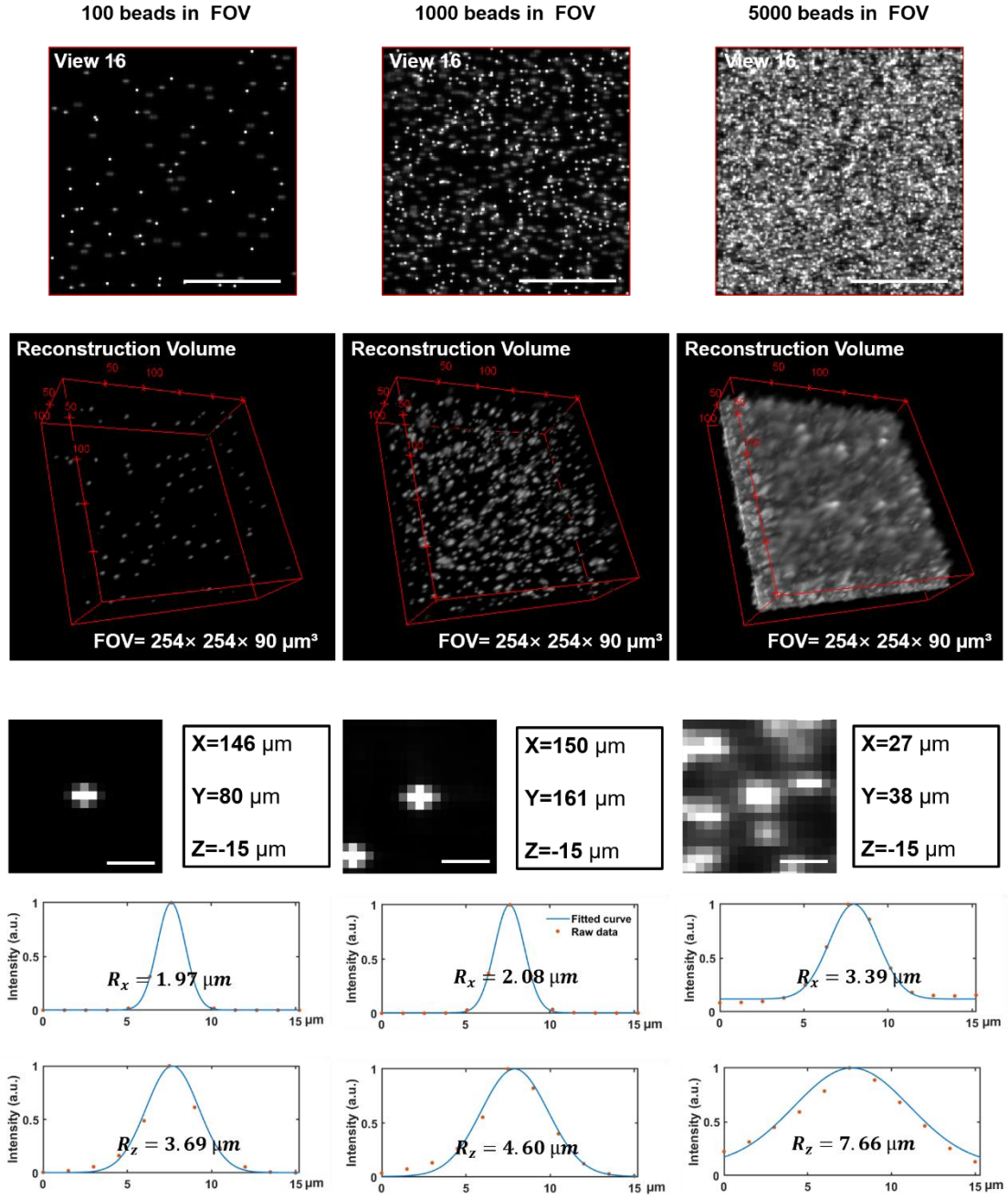
Fig. S23. Simulation of resolutions in samples of different densities. Scale bar: 100 μm in the view 16 images, and 10 μm in the enlarged beads images.
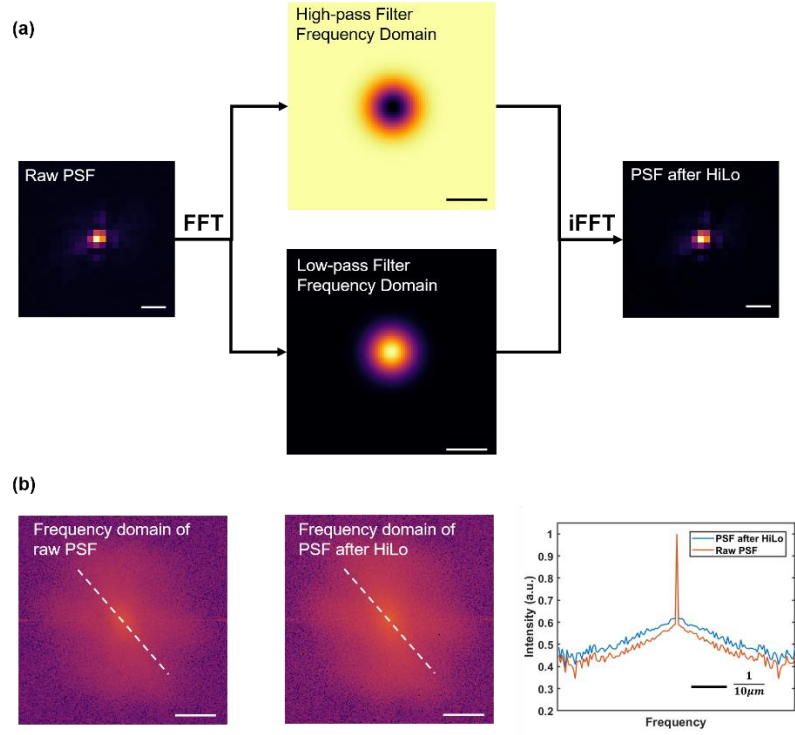
Fig. S24. Comparison between raw PSF and PSF after HiLo. $C_s(\vec{\rho})$=0.2, $\eta$=1.5. (a). HiLo process on PSF. (b). Comparison of frequency domain between raw PSF and PSF after HiLo, shown in log. Scale bar: 5 µm in PSF figures, $\frac{1}{15\ \mu m}$ in filter figures in Fig. S24a, $\frac{1}{50\ \mu m}$ in Fig. S24b.

**Supplementary Note 1: Design of RFLFM**

The design of RFLFM includes two parts: FLFM and HiLo.

**1.Design of FLFM**

FLFM provides volumetric imaging ability by dividing frequency spectrum to multi views, the imaging NA for each view is proportional to the size of each lens. To our applications, we need large field-of-view (FOV) and depth-of-field (DOF) for functional imaging, with relatively high resolution. However, many trade-offs must be concerned when designing FLFM[5, 6]. For instance, if we enlarge the lens, resolution will be improved but DOF decreased, meanwhile the focal length of MLA must be larger to ensure adequate sampling ratio (SR), which also reduces the FOV and usually hard to be manufactured. So here we discuss the relationships between the optical device and optical performance in detail and illustrate our design as example. The device parameters are listed in Table S1.

Table S1 Device parameters in RFLFM

| Device | Parameter | |
|---|---|---|
| Objective | $M$ (magnification) | 25 |
| | $NA$ (numerical aperture) | 1.05 |
| | $n$ (refraction index) | 1.333 |
| Relay lens (RL) | $f$ (focal length) | 150 mm |
| Tube lens (TL) | $f$ | 200 mm |
| Fourier lens (FL) | $f$ | 300 mm |
| Camera | Numbers | 5120 × 5120 |
| | Pixel size | 4.5 μm |
| MLA (microlens array) | $f$ | 38.24 mm |
| | Size | 3 mm ×4 mm |
| DMD (deformable mirror device) | Pixel size | 10.8 μm |
| | Numbers | 1920 ×1080 |

(1) Lateral resolution

The same as wide field microscopy, lateral resolution in FLFM is mainly determined by the diffraction limits. However, due to the segmentation of frequency spectrum, the imaging $NA$ is relatively smaller in FLFM. The lateral resolution can be estimated as:

$$R_x = \frac{\lambda}{2NA_{MLA}} = \frac{\lambda D}{2d_x NA_{obj}} \qquad (S-1)$$

Here, we note $R_x$ as lateral resolution, $NA_{MLA}$ as the imaging $NA$, $NA_{obj}$ as the $NA$ of objective, $D$ is the diameter of frequency spectrum on MLA plane, $d_x$ is the length or diameter of single microlens, and $\lambda$ is wavelength (520nm). $D$ can be calculated from the objective parameter and the relay system, for example, in our system, we use the 25×/1.05 (XLPLN25XWMP2, Olympus) objective, tube lens (AC508-200-A, Thorlabs) and Fourier lens (AC508-300-A, Thorlabs), so $D$ is

$\frac{180}{2\times1.05} \cdot \frac{300}{200} = 22.68$ mm. $d_x$ is 3mm in x direction, so $R_x = 1.87$μm, $R_y = 1.40$μm similarly.

However, *SR* is another important factor, which is connected to the magnification and camera pixel size, *SR* can be calculated by:

$$SR = \frac{M \cdot R_x}{d_{pixel}} \qquad (S-2)$$

Here, we note $M$ as the imaging magnification, and $d_{pixel}$ as the pixel length (4.5μm) of camera. In our system, $M$ is $\frac{25 \times 200}{180} \cdot \frac{38.24}{300} = 3.54$, $SR$ is only 1.47, which is smaller than Nyquist

sampling ratio of 2. To promise for adequate $SR$, the expected $R_x$ becomes $2 \times \frac{d_{pixel}}{M} = 2.54$μm, and the same as $R_y$. If $SR>2$, $R_x$ will become diffraction limits again.

(2) Axial resolution

Axial resolution is an important indicator for evaluating the volumetric imaging capability, which can be simply estimated by measuring the slope of three-dimensional PSF in $x$-$z$ projection (as shown in Fig. S5b), however, the theoretical prediction value is very important and always guide the experiments. Here, we introduce the theoretical derivation for axial resolution in our system.

The MLA is placed on the back focal plane of Fourier lens, so the different microlens accept different frequency component. We note the distance from each microlens (number i) center to the central optical axis as $d_i$. From the angular spectrum theory, the different spatial frequency component can be regarded as the light in different direction, so that analysis in geometric optics is permitted. An axial displacement $dz$ near native object plane (NOP) causes another axial displacement on native image plane (NIP) with $M_{obj}^2$ times magnification. In our system, it is $(\frac{25 \times 200}{180})^2 = 772$ times $dz$.

With a specific propagation direction $\theta_i$, the defocus equals a shift on NIP, the value is determined by $\theta_i$ and defocus value. The shift will be recognized as it exceeds the lateral resolution, therefore, the axial resolution in our system is:

$$R_z = \frac{R_x}{M_{obj} \cdot \theta_i} = \frac{R_x}{M_{obj}} \cdot \frac{f_{fourier\ lens}}{\max(d_i)} = 3.05 \ \mu m \qquad (S-3)$$

Where $f_{fourier\ lens} = 300$mm, and $\max(d_i) = 9$mm here. From where we can see, the higher $\theta_i$ is, the higher axial resolution could be achieved, to afford it, high NA objective and large size camera are recommended.

(3) FOV

The FOV is determined by the sensor size divided for each view and the imaging magnification $M$. To avoid unexpected mixing in neighboring views, we restrict the sub-image smaller than single microlens, in our system, we choose $d_x = 3$mm. Thus, our FOV is expected as:

$$FOV = \frac{d_x}{M} = 847 \ \mu m \qquad (S-4)$$

The larger microlens usually offer larger FOV, however, we must concern about the its focal length and $SR$ of camera to make sure the equipment fit.

(4) DOF

The DOF is dependent on the diffraction limit, which is inverse proportional to the square of $NA$. After segmenting the frequency domain, our imaging NA is only 0.1389, which suggests a large DOF could be acquired. The near focus intensity profile along central axis can be derived according to the wave optics theory, the DOF is represented as the FWHM of the above profile (which is about 1.75 times compare to the 80% intensity DOF), now the DOF is expected as:

$$DOF \approx 1.75 \frac{n\lambda}{(NA_{MLA})^2} = 62.8 \ \mu m \qquad (S-5)$$

As mentioned above, in our system, we can only achieve lateral resolution of 2.54 μm, however, it helps our DOF increase correspondingly, after multiplying a coefficient of $\frac{2.54}{1.87}$ to the DOF, the expecting DOF becomes 85.3μm, which is closely to the actual experiment applications.

The theoretical analysis can be used to estimate the optical performance of FLFM under different optical parameters.

(5) DOF and axial resolution

The DOF and axial resolution is connected by lateral resolution ($DOF \sim R_x{}^2, R_z \sim R_x$), here we discuss the relationship between them in two conditions:

① Firstly, the sampling ratio $SR>2$:

$$R_x = \frac{\lambda}{2NA_{MLA}} \tag{S-6}$$

$$DOF \approx 1.75 \frac{n\lambda}{(NA_{MLA})^2} = 1.75 \frac{n}{\lambda}(2R_x)^2 \tag{S-7}$$

$$R_z = \frac{R_x}{M_{obj}} \cdot \frac{f_{fourier\ lens}}{\max(d_i)} = R_x \cdot tg\theta \tag{S-8}$$

The $tg\theta$ can be measured by experiment (Fig. S16) or directly derived by the parameters. Based on these, DOF can be calculated by:

$$DOF \approx 1.75 \frac{n}{\lambda}(2\frac{R_z}{tg\theta})^2 = \frac{7n}{\lambda}(\frac{R_z}{tg\theta})^2 \tag{S-9}$$

For example, $R_x = 1.87$ μm, $tg\theta = 1.2$, $R_z = R_x \cdot tg\theta = 2.24$ μm, thus the $DOF = 62.8$ μm, which is equal to equation. (S-5).

② Secondly, the sampling ratio $SR \leqslant 2$:

$$R_x = \frac{2}{SR} \frac{\lambda}{2NA_{MLA}} \tag{S-10}$$

$$R_z = R_x \cdot tg\theta \tag{S-11}$$

$$DOF \approx 1.75 \frac{n}{\lambda} \frac{SR}{2}(2R_x)^2 = \frac{7n \cdot SR}{2\lambda}(\frac{R_z}{tg\theta})^2 \tag{S-12}$$

For example, $R_x = 1.87 \times \frac{2}{1.47} = 2.54$ μm, $tg\theta = 1.2$, $R_z = R_x \cdot tg\theta = 3.05$ μm, thus the $DOF = 85.3$ μm, which is equal to the final results in "(4) DOF".

**2.Design of HiLo**

The basic of HiLo has been illustrated clearly by Mertz[7, 8]. HiLo provides optical sectioning ability for wide field microscopy by calculating the contrast for the two raw images under different illumination ways. In RFLFM, the optical sectioning capability of HiLo should match the imaging DOF of the designed FLFM. Based on this, we must choose the grid pattern based HiLo rather than the speckle/diffuser based HiLo, since the modulated depth range is fixed in latter as the illumination DOF.

Here, we discuss the principle and data processing procedure for HiLo. We define $I_u(\vec{\rho})$ and $I_n(\vec{\rho})$ to represent the uniform illumination image and the structure illumination image, respectively, where $\vec{\rho}$ are the image coordinates.

The image contrast plays an important role in HiLo, which can be calculated as:

$$C(\vec{\rho}) = \frac{<\sigma(I(\vec{\rho}))>}{<I(\vec{\rho})>} \qquad (S-13)$$

Where the $<\sigma(I(\vec{\rho}))>$ and $<I(\vec{\rho})>$ represent for the standard deviation and average of the selected image. A full frequency image without background can be recovered in two steps. Firstly, as the defocus distance increase, the high frequency component attenuated more quickly[9], so the in-focus high frequency component can be extracted directly by doing a high pass filter to the uniform image $I_u(\vec{\rho})$:

$$I_{Hi}(\vec{\rho}) = HP(I_u(\vec{\rho})) \qquad (S-14)$$

Where HP represent for the high pass filter process with a cut-off frequency $k_c$ in frequency domain, and $k_c \leq k_{grid}$.

Then we need to extract the in-focus low frequency component. To concern about a thin-object, the $C_n(\vec{\rho})$ is nearly to 1 while the object is modulated by structure illumination, on the other hand, the $C_n(\vec{\rho})$ is nearly to 0 when the object is out-focus. Therefore, the value of $C_n(\vec{\rho})$ is on behalf of the proportion of the in-focus object in the object domain. However, the object is always non-uniform, which will induce contrast $C_o(\vec{\rho})$ during imaging, the illumination induced contrast $C_s(\vec{\rho})$ can be derived by:

$$C_n^2(\vec{\rho}) = C_o^2(\vec{\rho}) + C_s^2(\vec{\rho}) + C_o^2(\vec{\rho})C_s^2(\vec{\rho}) \qquad (S-15)$$

Where $C_o(\vec{\rho})$ can be calculated directly from the $I_u(\vec{\rho})$. After getting $C_s(\vec{\rho})$, the in-focus low frequency component could be obtained by applying the low pass filter to $I_u(\vec{\rho})$ while multiplying a coefficient $C_s(\vec{\rho})$:

$$I_{Lo}(\vec{\rho}) = LP(C_s(\vec{\rho}) \cdot I_u(\vec{\rho})) \qquad (S-16)$$

The total optical-sectioning image will be achieved by synthesizing from the fusion of the two raw images, resulting in:

$$I_{HiLo}(\vec{\rho}) = I_{Hi}(\vec{\rho}) + \eta I_{Lo}(\vec{\rho}) \qquad (S-17)$$

Where $\eta$ is a scaling factor used to make sure the low-pass and high-pass frequency information combined seamlessly. In our experiments, the $\eta$ are adjusted in the range of 0.6~1.0 for *in vivo* larval zebrafish samples and mouse samples.

# Supplementary Reference

1. Shi, R. and L. Kong, *Evaluating structured-illumination patterns in optimizing optical-sectioning of HiLo microscopy.* J Phys D: Appl Phys, 2021. **54**(41).

2. Lim, D., T. Ford, K. Chu, and J. Mertz, *Optically sectioned in vivo imaging with speckle illumination HiLo microscopy.* J Biomed Opt, 2011. **16**: p. 016014.

3. Broxton, M., L. Grosenick, S. Yang, N. Cohen, A. Andalman, K. Deisseroth, and M. Levoy, *Wave optics theory and 3-D deconvolution for the light field microscope.* Opt Express, 2013. **21**(21): p. 25418-39.

4. Zhang, Z., L. Bai, L. Cong, P. Yu, T. Zhang, W. Shi, F. Li, J. Du, and K. Wang, *Imaging volumetric dynamics at high speed in mouse and zebrafish brain with confocal light field microscopy.* Nat Biotechnol, 2021. **39**(1): p. 74-83.

5. Guo, C., W. Liu, X. Hua, H. Li, and S. Jia, *Fourier light-field microscopy.* Opt Express, 2019. **27**(18): p. 25573-25594.

6. Llavador, A., J. Sola-Pikabea, G. Saavedra, B. Javidi, and M. Martinez-Corral, *Resolution improvements in integral microscopy with Fourier plane recording.* Opt Express, 2016. **24**(18): p. 20792-8.

7. Neil, M.A.A., R. Juškaitis, and T. Wilson, *Method of obtaining optical sectioning by using structured light in a conventional microscope.* Opt Lett, 1997. **22**(24): p. 1905-1907.

8. Santos, S., K.K. Chu, D. Lim, N. Bozinovic, T.N. Ford, C. Hourtoule, A.C. Bartoo, S.K. Singh, and J. Mertz, *Optically sectioned fluorescence endomicroscopy with hybrid-illumination imaging through a flexible fiber bundle.* J Biomed Opt, 2009. **14**(3): p. 030502.

9. Dan, D., B. Yao, and M. Lei, *Structured illumination microscopy for super-resolution and optical sectioning.* Chin Sci Bull, 2014. **59**(12): p. 1291-1307.